Investigating the Understanding of Oxidation Chemistry Using 20 Years of Airborne OH and HO_2 Observations

David O. Miller[1], William H. Brune[1]

[1]Department of Meteorology and Atmospheric Science, Pennsylvania State University, University Park, PA, USA.

Corresponding author: David Miller (dom101@psu.edu)

Key Points:

- Observed and modeled OH and HO_2 generally agree throughout the free troposphere, based on analysis of nine airborne studies.
- Measuring more chemical species may not improve observed-to-modeled agreement for OH and HO_2, except in polluted or forested environments.
- Disagreements between observed and modeled OH and HO_2 are likely due to measurement issues and not the different models used.

Abstract

Hydroxyl (OH) and hydroperoxyl (HO_2) drive the atmosphere's oxidation of gases emitted from Earth's surface and the formation and aging of aerosol particles. Thus, understanding OH and HO_2 chemistry is essential for examining the impact of human activity on future atmospheric composition and climate. Using the OH and HO_2 dataset collected with the Penn State Airborne Tropospheric Hydrogen Oxides Sensor (ATHOS) during nine aircraft missions over the past 20 years, we compare observed OH and HO_2 to that modeled using the same near-explicit photochemical box model. In general, the agreement is well within the uncertainties of the observations and models, even when the model is constrained only with a common data set of simultaneous measurements. However, in regions influenced by anthropogenic or biogenic volatile organic compounds, the model chemical mechanism and size of the data set of constraining measurements do matter. In cleaner regions, the differences between observed and modeled OH and HO_2 found in previous studies generally remain and do not appear to be systematic, indicating that the differences are driven by measurement issues for ATHOS and/or other instruments. Thus, these comparisons indicate that the oxidation chemistry in most of the free troposphere is understood to as well as current measurements can determine. The focus of future research needs to be on regions rich in volatile organic compounds, where observed-to-modeled differences are more persistent, and on improving measurement consistency.

Plain Language Summary

Understanding the atmospheric chemistry that results in the removal of important greenhouse gases, such as methane, is critical in assessing the impact of human activity on future climate. Using airborne atmospheric data collected over a twenty-year period, we compare observed and modeled hydroxyl and hydroperoxyl, two important reactive gases, to evaluate our ability to model this oxidation chemistry. Overall, these comparisons show agreement between observed and modeled hydroxyl and hydroperoxyl to within instrument and model uncertainty, although the level of agreement degrades over polluted or forested regions, and is variable from mission to mission and even within missions. The lack of systematic disagreement between observed and modeled hydroxyl and hydroperoxyl when using the same model for all the studies suggests that unexpected variations in instrument performance is responsible for this variable level of agreement.

1 Introduction

Globally, the radicals hydroxyl (OH) and hydroperoxyl (HO_2), collectively known as HO_x, primarily drive atmospheric oxidation. OH oxidation is the primary pathway for the removal of gases emitted into the atmosphere (e.g., methane (CH_4), carbon monoxide (CO), non-methane hydrocarbons (NMHCs)) and it is involved in the production of ozone (O_3) and secondary organic aerosols (SOAs). Therefore, having a sound understanding of HO_x is critical to our knowledge of tropospheric chemistry (Ehhalt et al., 1990; Lelieveld et al., 2004).

OH and HO_2 are intrinsically linked through various chemical reactions (Jaeglé et al., 2000). Photolysis of ozone followed by the reaction of $O(^1D)$ with water vapor (H_2O) is the primary source of OH (Logan et al., 1981). Reactions of OH with CO produces HO_2, which can then react with itself to produce hydrogen peroxide (H_2O_2). Additional HO_x sources include the

photolysis of H_2O_2, formaldehyde (HCHO), nitrous acid (HONO), methylhydroperoxide (CH_3OOH), and acetone ($CH_3C(O)CH_3$). HO_x losses are primarily controlled by the abundance of NO_x ($NO_x = NO + NO_2$). Reactions of HO_2 and organic peroxyl (RO_2) with NO create NO_2. Photolysis of NO_2 produces NO and $O(^3P)$, the latter of which combines with O_2 to produce O_3. Therefore, the ultimate distribution of HO_x is highly dependent on the distribution of many trace gases and anthropogenic emissions.

OH lifetimes are typically a less than a second or two while HO_2 can survive for a few minutes, resulting in highly variable distributions of HO_x. Because of the relatively short lifetimes of HO_x and the influence of highly-variable trace gases, making routine HO_x observations is both difficult and vital. Several techniques of measuring tropospheric HO_x have been employed (Heard & Pilling, 2003) but only one technique can measure both OH and HO_2 with the same instrument: laser-induced fluorescence (LIF) at low pressure, also known as fluorescent assay by gas expansion (FAGE) (Hard et al., 1984; Stevens et al., 1994). The first airborne instrument to use this technique was the Penn State Airborne Tropospheric Hydrogen Oxides Sensor (ATHOS) (Faloona et al., 2004), which has measured OH and HO_2 during eleven missions. For this study we consider nine aircraft missions (Table 1) with three of these missions having multiple parts, resulting in 14 separate time studies, each three to six weeks long, for analysis. The missions cover a wide range of locations (Figure 1) and seasons.

Table 1. NASA DC-8 aircraft missions with OH and HO_2 observations for the nine missions used in this study. Papers covering the comparison of measured and modeled HO_x are included under the mission name.

Mission	When	Where	Why
SONEX Faloona et al. (2000); Jaeglé et al. (2000)	October – November, 1997	North Atlantic Flight corridor	Aircraft impact on upper tropospheric chemistry
PEM Tropics-B Davis et al. (2001); Tan et al. (2001); Wang et al. (2001); Ravetta et al. (2001)	March – April, 1999	Remote Pacific Ocean	Remote troposphere composition
TRACE-P Ren et al (2008)	February – April 2001	Southeast Asia	Tropospheric chemistry near pollution sources
INTEX-A Ren et al. (2008)	July – August, 2004	Eastern United States	Tropospheric chemistry near pollution sources
INTEX-B Adhikary et at. (2010)	March – May, 2006	(1) Northern Pacific (2) Gulf of Mexico; Southern US	(1) Transport of Asian pollution to North America (2) Pollution effects for Southern US and Mexico
ARCTAS	April – June,	(1) Arctic	(1) Arctic pollution

Olson et al. (2012); Ren et al. (2012)	2008	(2) Western Canada	(2) Effects of wildfires and oil extraction
DC3 Brune et al. (2018)	May – June, 2012	Central United States	Impact of deep convective clouds on chemistry
KORUS-AQ	May – June, 2016	South Korea and surroundings	Impacts of local and Southeast Asian pollution
ATom Brune et al. (2020)	August, 2016 – May, 2018	Pole-to-pole; south in Pacific; north in Atlantic	Typical global tropospheric chemistry

Comparison of observations with box models is routinely used to evaluate both the observations and models (see references in Table 1). For the missions evaluated in this study, observed and modeled OH and HO_2 generally agree to within the combined observation and model uncertainties. However, discrepancies between observed and modeled HO_x remain, a few that appear to persist from mission to mission and others that are seemingly random both within and between missions. The seemingly random discrepancies could result from changes in instrument performance or calibration or changes in models, treatment of input variables, or model chemical mechanisms.

The nine missions that are the focus of this study illustrate the variability of discrepancies between measured and modeled HO_x. Using a zero-dimensional, time-dependent photochemical box (lumped input) model developed at NASA Langley Research Center, Olsen et al. (2001) observed OH underprediction and HO_2 overprediction at high altitudes during PEM Tropics-B. In contrast, Ren et al., (2008) observed OH underprediction at low altitudes and HO_2 underprediction at high altitudes during INTEX-A. Olson et al. (2004; 2012) found HO_2 overprediction at all altitudes for TRACE-P and for ARCTAS. However, using a near-explicit photochemical box model, Brune et al. (2018) observed observation-to-model HO_2 agreement well within uncertainties at these altitudes. All of the authors (references in Table 1) provide potential explanations for these discrepancies. Brune et al. (2020) also provides a more unified discussion of the possible causes for these discrepancies including ATHOS calibrations, HO_x

interferences, model treatment errors, model chemical mechanism errors, and issues with the other observations used to constrain the model.

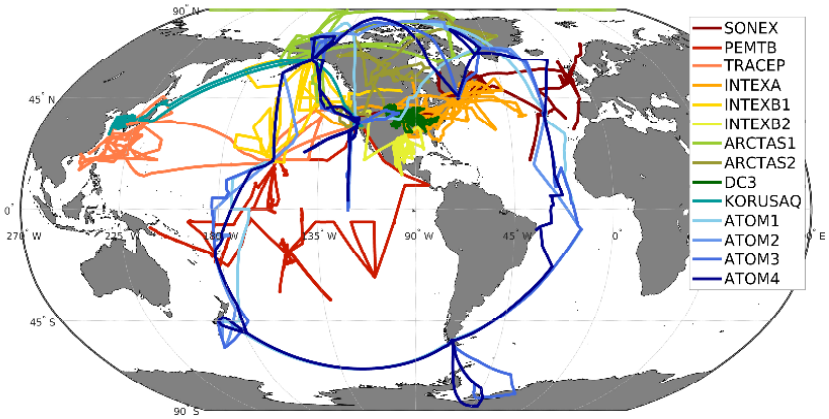

Figure 1. Flight tracks for all NASA DC-8 ATHOS missions used in this study. Note that ATom flight tracks frequently overlap. See Table 1 for more information about each mission.

This study aims to answer three questions about the general agreement between observed and modeled OH and HO_2 over the past two decades. First, is the variability in the OH and HO_2 comparisons from mission to mission due to using different model chemical mechanisms? Second, does using a near-explicit model chemical mechanism improve the agreement between observed and modeled OH and HO_2? Third, is the variability in the OH and HO_2 comparisons due to changes in the number and quality of simultaneous measurements of other chemical species used to constrain the model?

2 Measurements, Models, and Analysis Methods

This analysis leverages PSU ATHOS HO_x airborne observations in addition to an array of simultaneous observations over a two-decade timespan. For model comparisons to the publicly available OH and HO_2 datasets, we use the same model framework, near-explicit mechanism, and filtering and interpolation methods for all missions. The focus of this paper is on the median agreement between observed and modeled OH and HO_2. A second paper will focus on detailed comparisons.

2.1 HO_x Observations

For all the missions used in this study, OH and HO_2 were measured with the Penn State ATHOS instrument (Faloona et al., 2004). Briefly, sample air is pulled through a conical pinhole (~1.5 mm) inlet into a low-pressure environment between 3 hPa and 12 hPa depending on altitude. The sample air continues through a flow tube to the two detections axes. Each axis is composed of a multi-pass White cell where a 308 nm laser pulse (3 kHz repetition rate, 20 ns pulse length) passes ~32 times. OH absorbs the laser radiation and fluoresces and this signal is measured via a gated microchannel-plate detector.

Prior to the sample air entering the second detection axis, reagent nitric oxide (NO) is mixed with it to convert HO_2 to OH, which is then detected in the same manner as in the first axis. The laser is tuned on and off the OH resonance wavelength and the OH fluorescence signal

is the difference between these signals. The times the laser spends on and off resonance changed from mission to mission but the typical measurement time resolution was either 20 or 30 s. ATHOS was installed in the forward cargo bay of the NASA DC-8 aircraft with the inlet nacelle extending below the aircraft and the detection axes, laser system, and pumps were located within the cargo bay. Even with incremental improvements and upgrades, the core ATHOS instrument has not fundamentally changed over the timespan of the missions used in this study. Therefore, we do not expect any substantial change in HO_x detection performance.

The ATHOS calibration is performed using the process detailed in Faloona et al. (2004). OH and HO_2 are produced in equal amounts via water vapor photolysis at 184.9 nm. The absolute OH and HO_2 mixing ratios were calculated using the measured photon flux and H_2O mixing ratio, H_2O absorption cross section, and the exposure time of the water vapor to the UV light. Different conical pinhole inlets were used to change the internal pressure of ATHOS during the calibration sequence to simulate the effects of different measurement altitudes. Calibrations were performed before and after each mission in the laboratory and also in the field during each mission. The absolute calibration uncertainty was estimated to be ±32% for both OH and HO_2 at the 2σ confidence level (Brune et al. 2018) prior to KORUS-AQ, when OH and HO_2 potential interference remediation methods were implemented, resulting in overall OH and HO_2 uncertainties of ±35% at the 2σ confidence level for KORUS-AQ and ATom (Brune et al., 2020).

OH and HO_2 calibrations were re-examine for all previous missions using the most up-to-date software for converting count rates into mixing ratios. No changes were identified for the previous calibrations, with one exception. For HO_2 in ARCTAS, the INTEX-B calibration was inadvertently applied to the data instead of the ARCTAS calibration, with the ARCTAS calibration being a factor of 1.5 smaller. Thus, the ARCTAS HO_2 values in this study are now 1.5 times larger than reported in Olson et al. (2012). This change increases the observed-to-modeled HO_2 ratio to ~1.8 below 2 km in the planetary boundary layer for ARCTAS-B flights over Canada,. However, it resolves the issues raised in that paper concerning the 0.61 ratio for all of ARCTAS-A and ARCTAS-B at altitudes above 2 km, which were in fairly clean air where the chemistry should be understood.

In locations with high levels of alkenes and aromatics, interferences in OH (Mao et al., 2012) and HO_2 (Fuchs et al., 2011) observations have been identified. The magnitude of these interferences is primarily an issue within the planetary boundary layer (PBL) and above forests and cities. The vast majority of locations investigated in this study occur outside these areas of concern (Brune et al., 2020). However, corrections for these interferences based on VOC observations and modeled RO_2 have been identified (Ren et al., 2012; Brune et al., 2018) and were applied to all mission HO_x observations prior to KORUS-AQ.

The mitigation of these interferences was directly addressed in preparation for the KORUS-AQ mission due to the expected high levels of potential HO_x interference species. First, analysis of ground-based data (Feiner et al., 2016) and laboratory tests were performed to investigate the optimal reagent NO flow for converting HO_2 to OH while minimizing the conversion of RO_2 to OH. It was found that if the HO_2 conversion efficiency was < 30% then the interference becomes negligible. A 0.5 sccm flow of NO achieved a 28% conversion efficiency. In addition, a 7.0 sccm flow of NO converts all HO_2 to OH also allows some RO_2 species to be detected Therefore, starting with the KORUS-AQ mission, the NO flow was constantly stepped among 0, 0.5, and 7.0 sccm.

Second, an external injector was developed to scavenge OH upstream of the ATHOS pinhole inlet. The OH Scrubber Inlet (OHSI, Brune et al. (2020)) injects a mixture of nitrogen (N_2) and hexafluoropropylene (C_3F_6), an OH reactant, via four concentric capillary tubes upstream of the conical pinhole inlet. The N_2+C_3F_6 mixture is injected at sufficient flow to promote good mixing with the sample air. Laboratory and field tests reveal that 91±5% of the OH is removed from the sample air when the OHSI is operating, so that any remaining OH signal is an interference and is subtracted.

2.2 DC-8 Instrument Payloads

ATHOS has been deployed exclusively on the NASA DC-8 aircraft. While the instrument payload for each mission has changed over the years (Table S1), it always included measurements of methane, ozone, peroxides (e.g., H_2O_2, CH_3OOH), formaldehyde (HCHO), nitric acid (HNO_3), sulfur dioxide (SO_2), benzene, toluene, ethyl nitrate ($C_2H_5NO_3$), alkynes (e.g., C_2H_2), alkanes (e.g., C_3H_8), methyl nitrate (CH_3NO_3), peroxyacetyl nitrate (PAN), and standard meteorological variables (e.g., temperature, pressure, H_2O, and photolysis frequencies). While nitric oxide (NO) and nitrogen dioxide (NO_2) were always measured, issues with NO during INTEX-A and NO_2 during SONEX prevent their use for these missions and they are calculated from NO_x photostationary state. Of note in Table S1 is the general increase in the number of available measurements over the years.

2.3 Model Description

Various photochemical box models have been used over the years to compare with HO_x observations (Table 2). One goal of this study is to use the same model as a transfer standard between all mission comparisons to put the results on the "same page". To this end, the Framework for 0-D Atmospheric Modeling, version 4 (F0AMv4), was used for all observation-to-model comparisons (Wolfe et al., 2016). F0AM is a Matlab-based framework to facilitate the use of various chemical mechanisms. The primary mechanism used in this study is the Master Chemical Mechanism (MCM), version 3.3.1 (Saunders et al., 2003; Jenkin et al., 2003). MCM is a near-explicit chemical mechanism allowing for hundreds of input constraints and containing thousands of reactions. In addition, based on the findings by Assaf et al. (2017), the reactions $CH_3O_2 + OH = CH_3O + HO_2$ and $C_2H_5O_2+OH = C_2H_5O+HO_2$ and are added to the core set of MCM reactions.

For a set of simultaneous model input species at a given point in time, a model integration time of 24-hours was used for the computed chemical species concentrations, although tests show that the exact choice of integration time changed modeled OH and HO_2 insignificantly. The model was constrained with available observations of chemical species and photolysis frequencies (Table S1), and meteorological variables. The constraining observations were pulled from the merge files for each respective mission and interpolated to a common 1-minute interval. Frequently, gaps existed in observation data due to instrument calibrations or faults. A linear interpolation scheme was used to fill observation gaps of 15 minutes or less. Gaps remaining after interpolation were removed from the analysis. An effective surface deposition of 1.1×10^{-5} s^{-1} was used for all model runs, although the choice of this value had little impact on modeled OH and HO_2.

Both observations and model results are filtered prior to any comparisons. These filters include requiring O_3, NO, NO_2, HCHO, H_2O_2, CO, CH_4, photolysis frequencies, and meteorological variables be present and the observations to be within ±4 hours of local noon. OH

and HO_2 observations and model results must be above the limit of detection of 0.018 pptv and 0.2 pptv, respectively (Brune et al., 2020). Additionally, take-off and landing times were excluded by limiting altitudes to > 100 m and O_3 values > 150 ppbv were assumed to be stratospherically influenced and were removed.

Several metrics were used to evaluate the agreement between observed and modeled OH and HO_2. The slope, intercept, and R^2 from the York fit (York et al., 2004) to the scatterplots of the data and the percent difference (PD), defined by equation 1, were determined.

$$\mathrm{PD} = 100 \times \frac{(\mathrm{observation} - \mathrm{model})}{(\mathrm{observation} + \mathrm{model})/2} \quad (1)$$

For the SONEX through ARCTAS missions, observation-to-model comparisons already exist (Table 2). The models used in these comparisons lumped input variables into functional groups. By comparing the results from previous studies with those from this study the impact of using a near-explicit chemical mechanism was tested.

This study affords us with the opportunity to explore the impact of the changing instrument payloads (i.e., model input constraints) on modeled HO_x. For the earliest mission SONEX, 32 available chemical species observations were used to constrain the model in this study while the KORUS-AQ mission had 66 available chemical observations. To test the effects of the increasing number of observations from later missions, the model was also run restricting the observation inputs to only those species available for all missions (Table S1, dark gray rows).

Table 2. Photochemical box models used in previous analyses of the missions used in this study. For DC3, KORUS-AQ, and ATom, the current version of F0AM was used for analysis.

Mission	Model	Type	Reference
SONEX	Harvard 0-D diurnal steady-state model	lumped	Jaeglé et al., (2000)
PEM Tropics-B	Penn State 0-D steady-state	lumped	Crawford et al., (1999)
TRACE-P	NASA LaRC	lumped	Olson et al., (2004)
INTEX-A	NASA LaRC	lumped	Olson et al., (2004)
INTEX-B	NASA LaRC	lumped	Olson et al., (2004)
ARCTAS	NASA LaRC	lumped	Olson et al., (2006)
DC3, KORUS-AQ, ATom	F0AM / MCM	near explicit	Wolfe et al., (2016)

2.4 Violin Plots

Some results are visualized using violin plots (Hintze & Nelson, 1998). A violin plot is similar to a box-and-whisker plot, which typically shows the five-number summary statistics: the sample minimum, first quartile, median, third quartile, and maximum. However, the violin plot has a kernel density estimator to show the distribution of sample data. The wider the violin the more frequently that value occurs in the sample data.

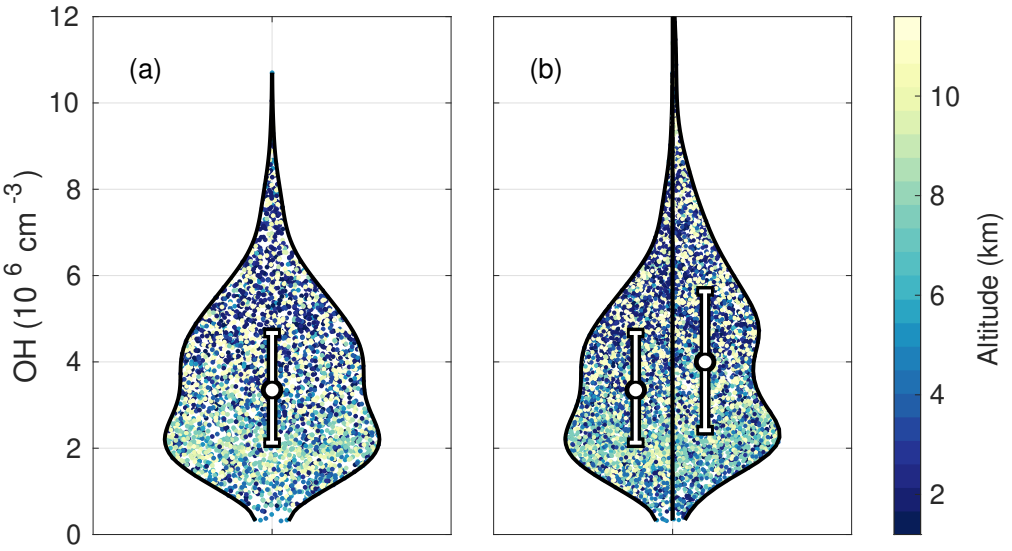

Figure 2. Example of a violin plot. (a) A violin plot showing the distribution of observed OH values for the DC3 mission. The median value is marked by the white circle and the bars indicate the 20% estimated uncertainty range of the observations. The point colors indicate altitude. The width of the violin represents the relative frequency of OH values. (b) A split violin plot showing observed OH (left) and MCM modeled OH (right) for the DC3 mission. The median values are marked by white circles and bars representing ±20% uncertainty of the observed and model values. The dot colors indicate altitude.

Figure 2a shows the observed OH from the DC3 mission covering a range of 0-10.8×10^6 cm^{-3}. The widest part of the violin, occurring at ~2.2×$10^6$$cm^{-3}$, indicates the most frequent value. The individual point colors correspond to altitude revealing the altitude dependence of the observations. For instance in Figure 2a, OH values greater than ~4×10^6 cm^{-3} tend to occur in the lowest few km whereas OH values of ~2×$10^6$$cm^{-3}$ tend to occur in the 5-10 km altitude range. The median value is indicated by a white circle. Two variations of the violin plot bars are used in the following sections. The bars indicate either the 20% uncertainty ranges for observed and modeled OH and HO_2 or the 25th and 75th percentiles of the percent differences for other cases. The use of the bars is noted in each figure caption.

A split violin is also used to compare two sets of samples. The left side of Figure 2b contrasts the same OH observations as Figure 2a with modeled OH shown on the right. The distribution of modeled OH is shifted towards larger values compared to measured OH. All of

the split violins have a vertical line dividing the two halves.

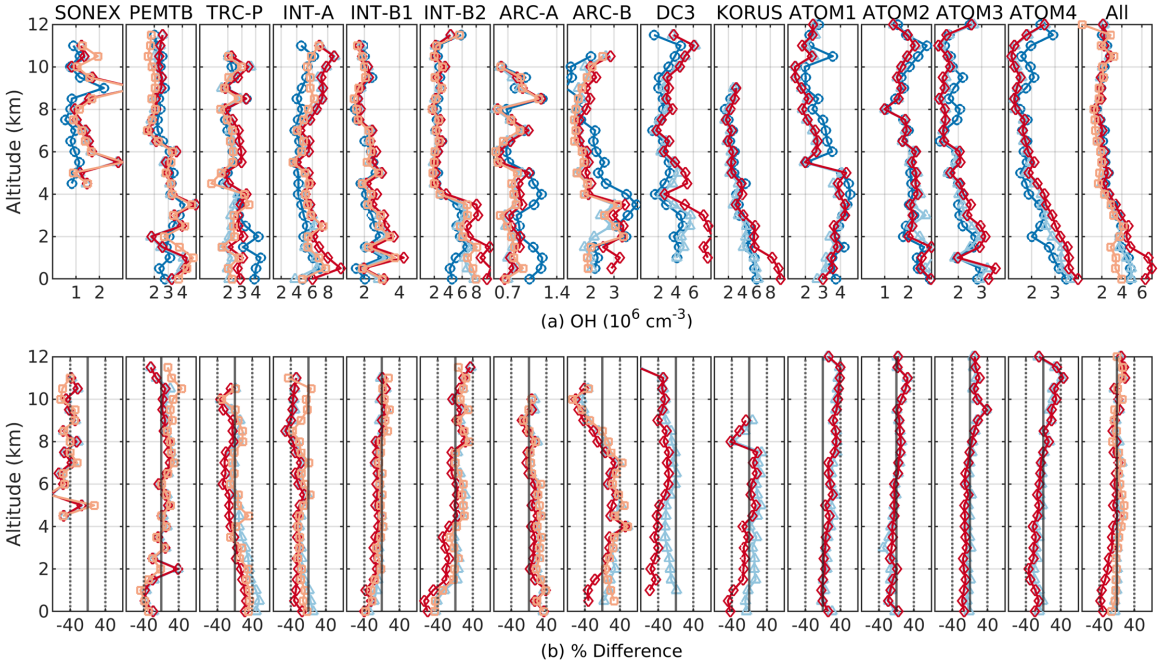

Figure 3. Observed and modeled OH vertical profiles. (a) Vertical profiles, averaged into 500 m bins, of OH observations (dark blue circles), MCM (light blue triangles), previous analysis (orange squares), and MCM (common input set, red diamonds) for all missions. The rightmost panel shows the median values for all missions. (b) Percent difference between OH observations and MCM (light blue triangles), previous analysis (orange squares), and MCM (common input set, red diamonds). The vertical dashed lines at -40 and +40 represent the combined observation and model uncertainties. The rightmost panel shows the median values for all missions.

3 Results

3.1 Comparisons of Observed and Modeled HO_x

A general sense of the agreement between observed and modeled OH can be gleaned from median altitude profiles. Altitude has the greatest influence on HO_x because of the combined effects of changing meteorological variables and chemical composition. Figure 3(a) shows altitude profiles of OH observations averaged in 500 m bins (dark blue circles) and MCM modeled OH (light blue triangles). Median OH varies from 0.5×10^6 cm^{-3} during ARCTAS-A to greater than 6×10^6 cm^{-3} during INTEX-A. Modeled OH captures the overall behavior of observed OH with some exceptions visible in vertical profiles of percent difference shown in Figure 3(b). While the percent differences (PDs, eq. 1) reveal that observed to modeled differences are generally within the combined uncertainties, some notable differences appear for the following cases: most altitudes during SONEX, lower altitudes during TRACE-P, INTEX-A, INTEX-B2, upper altitudes during INTEX-A, INTEX-B2, KORUS-AQ, ATom-1, and middle altitudes during ARCTAS-B. In the rightmost panel, the median observed and modeled OH profiles for all missions combined are well within the combined uncertainties. The comparisons between observations and different models are discussed in detail in the following sections.

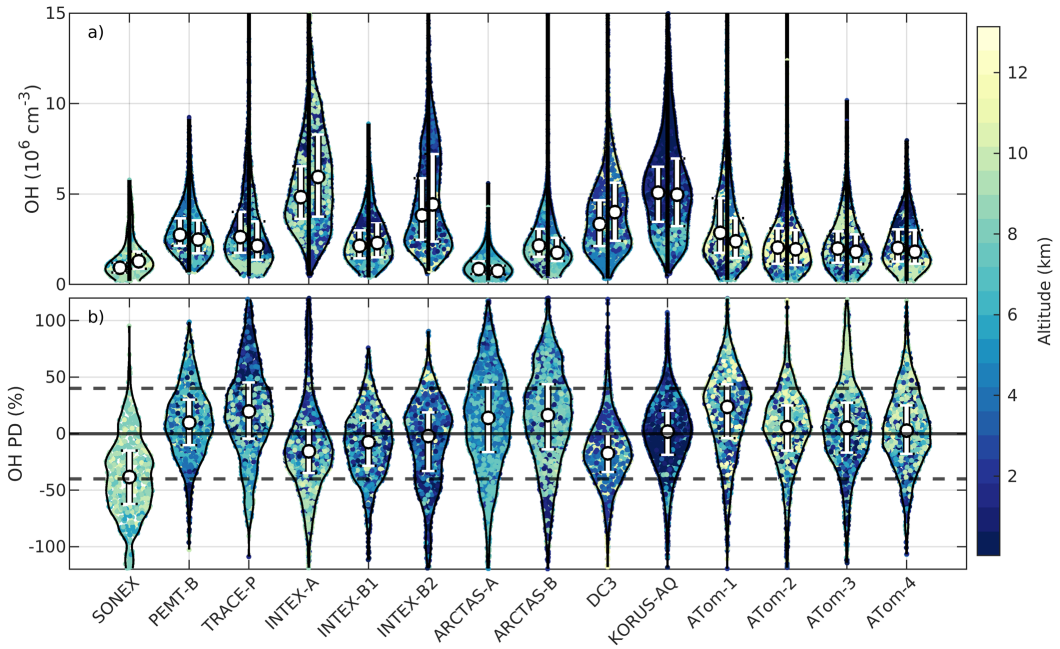

Figure 4. Violin plots of observed and modeled OH. a) Observed OH (left violins) and MCM modeled OH (right violins) for all missions. Median values (white circles) with bars indicating 25th and 75th percentiles. Point colors correspond to altitude. b) Percent difference (PD) between observed and MCM modeled OH for all missions. The horizontal dashed lines at −40% and +40% indicate the combined observation and model uncertainties.

Violin plots of the observed OH (left violins) and modeled OH (right violins) as a function of altitude (colored points) are shown in Figure 4(a). The median values (white circles) with bars indicating ±20% median uncertainty. A wide variety of environmental conditions were encountered over all the missions included in this study, as can been seen in the wide range of OH values. The greatest OH concentrations tend to occur in the planetary boundary layer (PBL), which is represented by the dark blue color. The two sides of each violin exhibit similar distributions and median values (white circles) being relatively similar although some exceptions are notably present with INTEX-A, INTEX-B2, and KORUS-AQ. Because of the generous overlap of the uncertainty ranges for observed and modeled OH, the median observed and modeled values are not statistically different.

The percent difference, PD, between the observations and model for each mission is shown in Figure 4b. The median PD for each mission lies within the combined observation and model uncertainties, however, SONEX has a median very close to the -40% percent difference. Also, for all missions, at least 17% of the points, with nearly 50% for SONEX, reside outside the combined uncertainties, whereas for a normal distribution, the amount outside would be only 10%. The altitude-dependent coloration on the OH PD violin plots echoes the PD shown in Figure 3b, such as the negative PD values for low altitudes in INTEX-A.

Figure 5a shows vertical profiles, averaged into 500m bins, of HO_2 for all of the missions with the median HO_2 profiles shown in the rightmost panel. The model captures the overall behavior of HO_2 with altitude. For SONEX, the PD for HO_2 is as low as it is for OH, whereas the remaining missions show good agreement with a few exceptions. Vertical PD profiles shown in

(Figure 5b) reveal that differences are mostly within the combined uncertainties. The median percent difference is close to zero over all altitudes.

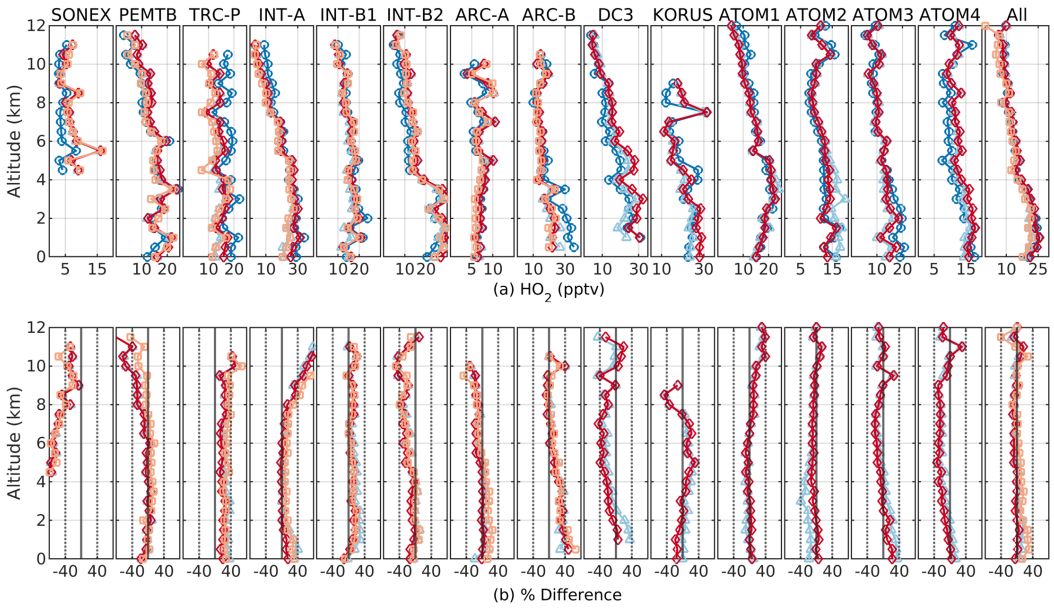

Figure 5. Observed and modeled HO_2 vertical profiles. (a) Vertical profiles, averaged into 500m bins, of HO_2 observations (dark blue circles), MCM (light blue triangles), previous analysis (orange squares), and MCM (common input set, red diamonds). The horizontal dashed lines at −40% and +40% indicated the combined observation and model uncertainties. (b) Percent difference between HO_2 observations and MCM (light blue triangles), previous analysis (orange squares), and MCM (common input set, red diamonds). The vertical dashed lines at -40 and +40 represent the combined observation and model uncertainties.

Comparing the observed and modeled HO_2 in Figure 6a reveals that both have similar distributions and medians. A much stronger altitude dependence is revealed compared to OH. As is the case with OH, there is considerable overlap in the $\pm$20% uncertainty ranges for HO_2 for all missions. The PDs between the observed and modeled HO_2 are shown in Figure 6b. The median PDs for all missions lies within the combined observation and model uncertainties. Only SONEX and TRACE-P have PD quartiles that lie outside the combined uncertainties.

Subtle differences in the distribution shapes of OH are seen, especially for INTEX-A, INTEX-B2, and DC3. There is a slight altitude dependence on OH PDs for TRACE-P, INTEX-A and ATom-1 and ATom-3, although in the first two, the PDs are more positive for lower altitudes whereas for the last two, the PDs are more positive for higher altitudes. For HO_2, altitude differences in the PDs are obvious for PEM Tropics-B, INTEX-A, DC-3, and ATom-1.

Table S2 provides the OH statistics including the slope, intercept, R^2 from the York fit between the observations and model results, the median ratio and percent difference between the observations and model results, the number of data points from each mission used in the analysis, and the number of data points within a percent difference of ±40% which corresponds to combined observation and model uncertainties. The median slope, intercept, and R^2, for all missions, are 0.97, 0.07×10^6 cm^{-3}, and 0.64, respectively. The median ratio and percent difference, between observed and modeled OH, are 1.01 and 1.12%, respectively. Overall, 71.7% of the 32393 data points used from all missions are within a percent difference of ±40%.

However, the slopes range from 0.63 for INTEX-A to 1.34 for ARCTAS-A and ATom-1 and the intercepts range from -0.18×10^6 cm^{-3} for ATom-1 to 1.08 × 10^6 cm^{-3} for INTEX-A. R^2 values range from 0.24 for ARCTAS-B to 0.75 for SONEX. Median ratios of observed to modeled OH range from 0.68 for SONEX to 1.27 for ATom-1. The median percent difference varies from -38.6% for SONEX to 23.9% for ATom-1. The number of data points range from 558 for SONEX to 5392 for KORUS-AQ. Finally, the fraction of times with PDs within ±40% varied from 50.2% for SONEX to 82.3% for KORUS-AQ. Overall for OH, the PD is less than ±10% for 8 missions, greater than 10% for 4 missions, and less than 10% for 3 missions.

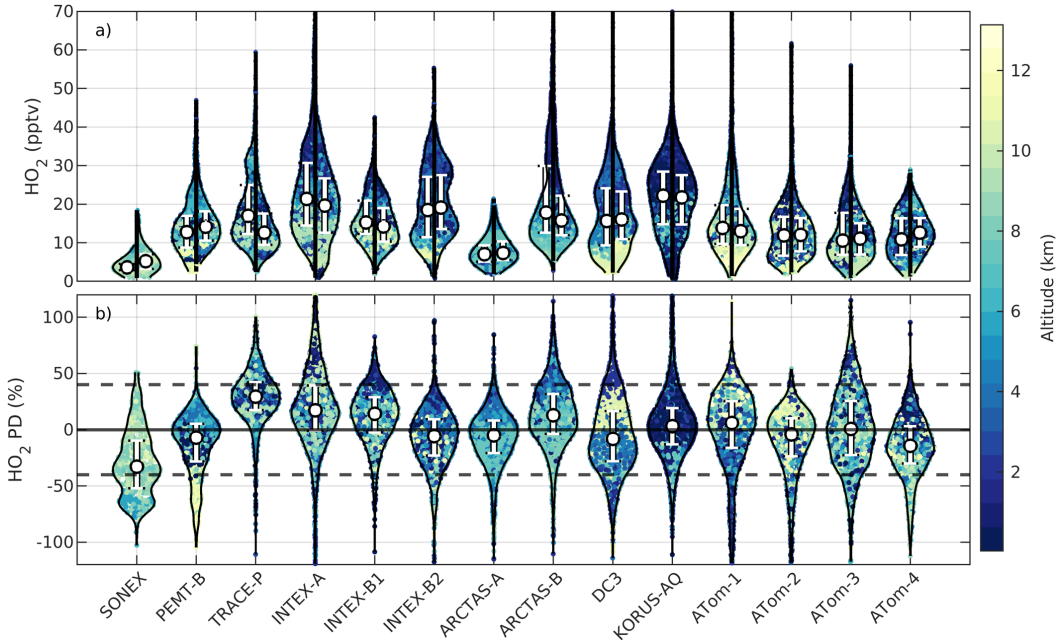

Figure 6. Observed and modeled HO_2 violin plots. a) Observed HO_2 (left violins) and MCM modeled HO_2 (right violins) for all missions. Median values (white circles) with bars indicating 25th and 75th percentiles. Point colors correspond to altitude. b) Percent difference (PD) between observed and MCM modeled HO_2 for all missions. The horizontal dashed lines at −40% and +40% indicate the combined observation and model uncertainties.

Table S3 provides the statistics for HO_2. The median slope, intercept, and R^2, for all missions, are 1.07, -0.46 pptv, and 0.63, respectively. The median ratio and percent difference, between observed and modeled HO_2, are 1.03 and 2.56%, respectively. Overall, 80.3% of the 32393 data points used from all missions are within a percent difference of ±40%. However, the slopes range from 0.48 for SONEX to 1.44 for TRACE-P and ARCTAS-B and the intercepts range from -4.50 pptv for PEM Tropics-B to 3.60 pptv for INTEX-A. R^2 values range from 0.37 for ATom-1 to 0.84 for PEM Tropics-B. Median ratios of observed to modeled HO_2 range from 0.72 for SONEX to 1.35 for TRACE-P. The median percent difference varies from -32.96% for SONEX to 29.6% for TRACE-P. Finally, the fraction of times with PDs within ±40% varied

from 60.0% for SONEX to 90.5% for ARCTAS-A. Overall for HO_2, the PD is less than ±10% for 9 missions, greater than 10% for 4 missions, and less than 10% for 2 missions.

3.2 Impact of Model Chemical Mechanism

We can compare the OH from MCM chemical mechanism to OH from the lumped chemical mechanisms that were primarily used for modeling OH and HO_2 before DC3 (Figure 3(a)). The lumped models used in these studies (Table 2) perform similarly to the MCM model (light blue triangles) for most of the missions, even mirroring discrepancies with observations at some altitudes. The vertical PD profiles are shown in Figure 3(b) revealing essentially no difference between the lumped and MCM model results.

Comparison of OH modeled using MCM (left violins) and from previous studies (right violins) is shown in Figure 7(a) where the circles represent the median OH and the error bars represent the respective model uncertainty of ±20%. Because the range of uncertainty overlaps for all missions the medians cannot be confirmed to be different. The PDs between observed and modeled OH are shown in Figure 7(b) with MCM on the left and previous studies on the right. The error bars represent the 25th and 75th percentiles of percent difference. The median values from the previous studies also reside within the combined observation and model uncertainties for all missions.

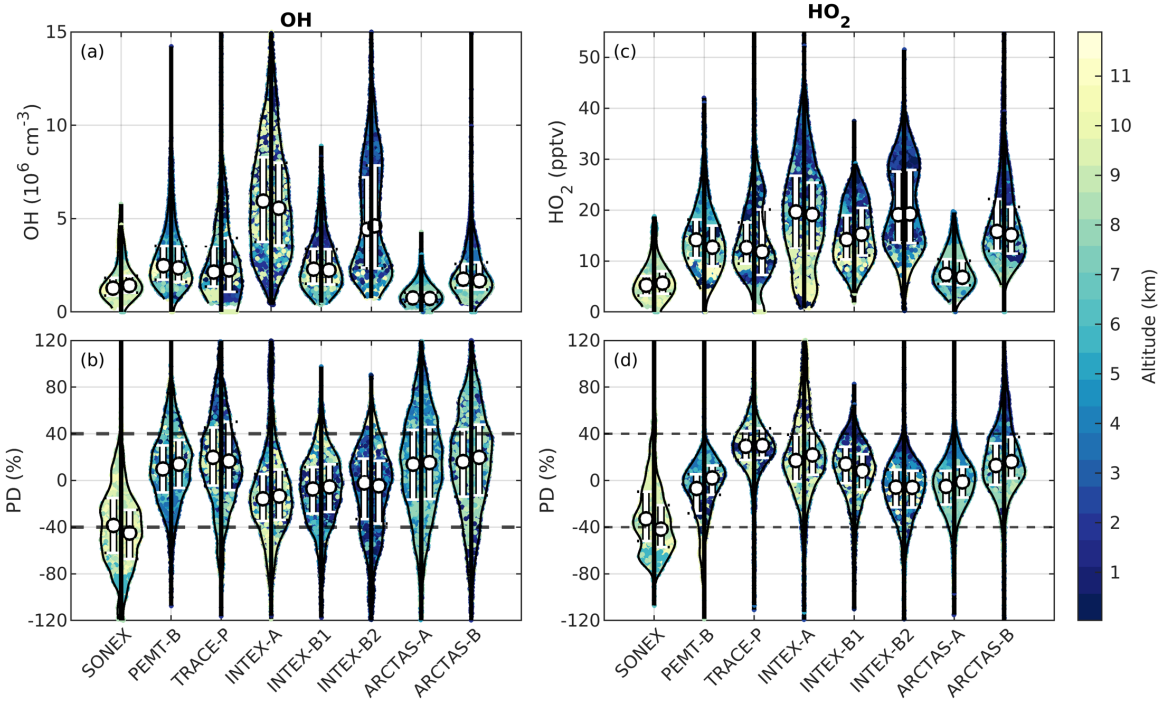

Figure 7. Violin plots of modeled OH and HO_2 with MCM and prior lumped mechanism models. Shown are modeled OH (a) from MCM (left violins) and previous studies (right violins); OH PD (b); modeled HO_2 (c) and HO_2 PD (d). The white circles represent the median and the error bars represent the model uncertainties of ±20%.

Table S2 also includes the OH statistics from previous studies indicated by the 'Prev' rows. The median slope, intercept, and R^2 is 0.92, 0.15 x10^6 cm^{-3}, and 0.71, respectively. The

median ratio and percent difference are 1.03 and 2.92%, respectively. 65.3% of the 15299 data points from SONEX through ARCTAS-B are within the ±40% combined uncertainties. However, the slopes range from 0.64 for INTEX-A to 1.17 for ARCTAS-A. Intercepts range from -0.10x10^6 cm^{-3} for SONEX to 1.12 x10^6 cm^{-3} for INTEX-A. R^2 values range from 0.28 for ARCTAS-B to 0.66 for INTEX-B1. Median ratios range from 0.63 for SONEX to 1.22 for ARCTAS-B. Median percent differences range from -44.9% for SONEX to 19.6% for ARCTAS-B. The fraction of times with PDs within ±40% varied from 40.5% for SONEX to 81.3% for INTEX-B1.

Comparisons of HO_2 modeled using MCM (left violins) and from previous studies (right violins) is shown in Figure 7(c) where the circles represent the median HO_2 and the error bars represent the model uncertainty of ±20%. As for OH, modeled HO_2 using MCM is essentially the same as the results from previous studies. However, there are noticeable differences in the distributions of HO_2 values for TRACE-P and INTEX-A. The percent differences between observed and modeled HO_2 are shown in Figure 7(d) and reflect essentially the same performance between the models.

Table S3 also shows the statistics for previous studies (rows marked 'Prev') for HO_2. The median ratio and percent difference are 1.10 and 9.16%, respectively. 79.6% of the 15299 data points from SONEX through ARCTAS-B are within the ±40% combined uncertainties. However, the slopes range from 0.42 for SONEX to 1.45 for ARCTAS-B. Intercepts range from –3.05 pptv for ARCTAS-B to 6.28 pptv for TRACE-P. R^2 values range from 0.58 for TRACE-P to 0.82 for PEM Tropics-B. Median ratios range from 0.65 for SONEX to 1.36 for TRACE-P. Median percent differences range from -41.8% for SONEX to 30.2% for TRACE-P. The fraction of times with PDs within ±40% varied from 43.0% for SONEX to 94.1% for ARCTAS-A. The median slope, intercept, and R^2 is 1.08, 0.13 pptv, and 0.69, respectively.

3.3 Impact of Input Data Set

Comparing observed OH and HO_2 with different model mechanisms but a common constraining input data set provides some insight into the sensitivity of the comparison of observed and modeled HO_x to the input data. Figure 3(a) also shows vertical profiles of OH, binned every 500m, of the MCM results using the common input data set (red diamonds). Overall, the MCM model continues to perform well with fewer constraining inputs but differences emerge at lower altitudes for INTEX-A, INTEX-B2, ARCTAS-B, DC3, and KORUS-AQ, all missions in which a substantial number of samples were taken in air affected by anthropogenic or biogenic emissions. These differences are also revealed in the PD profiles in Figure 3(b).

The comparisons of MCM modeled OH using the full versus common input data set are shown in Figure 8. OH increased with the common input set for all missions (Figure 8(a)) which correspondingly shifted the PDs between the observed and modeled OH. The greatest differences in PDs and in the shapes of the frequency distributions were for INTEX-A, INTEX-B2, DC3, and KORUS-AQ. The percent differences were higher for the full dataset than for the common data set, but they were closer to zero for less than half the missions.

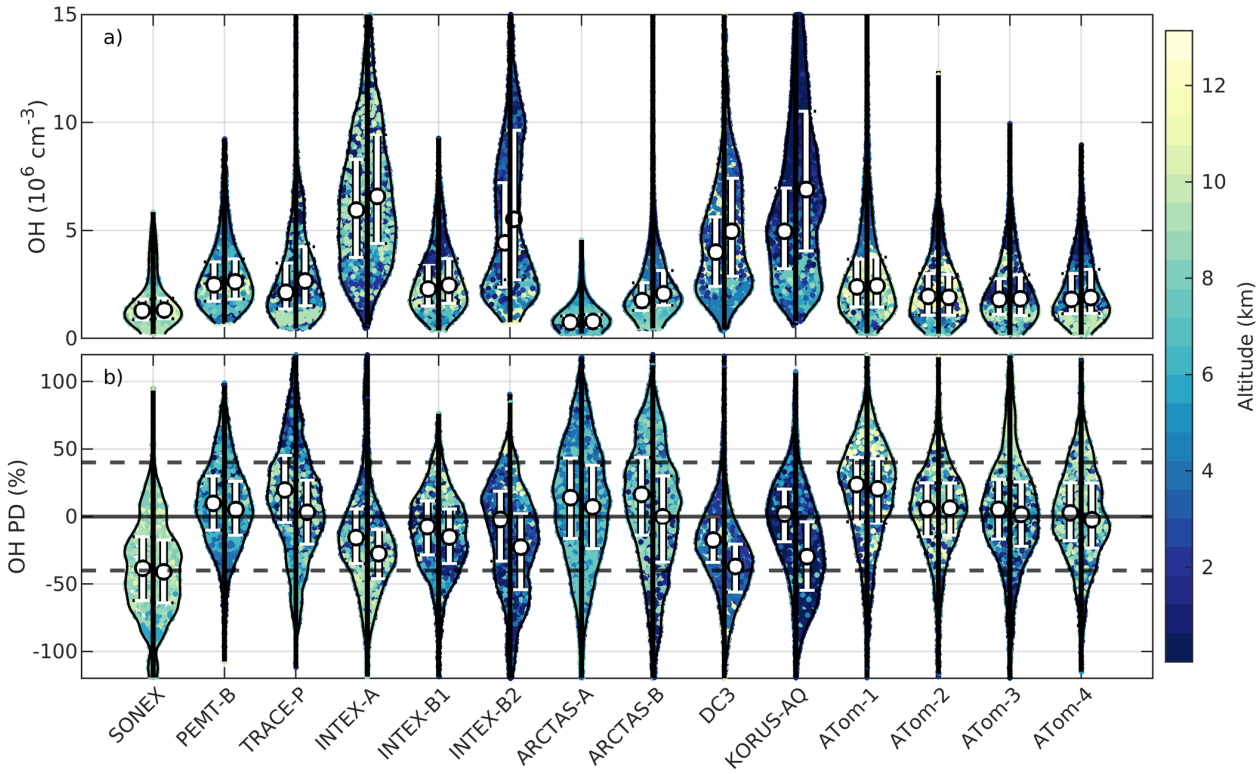

Figure 8. Violin plots of modeled OH, without and with common input constraints. (a) Modeled OH from MCM (left violins) and MCM with common input set (right violins). The white circles represent the median and the error bars represent the model uncertainties of ±20%. (b) Percent difference between observed and modeled OH using MCM (left violins) and MCM with common input set (right violins). The bars represent the 25th and 75th percentiles of PD.

Table S2 also includes the OH statistics from the common input set model runs indicated by the numbers in parentheses. The median slope, intercept, and R^2 is 0.80, 0.15 $x10^6$ cm^{-3}, and 0.65, respectively. The median ratio and percent difference are 0.88 and -12.7%, respectively. 64.4% of the 32393 data points are within the ±40% combined uncertainties. However, the slopes range from 0.57 for KORUS-AQ to 1.27 for ATom-1. Intercepts range from -0.10$x10^6$ cm^{-3} for ATom-1 to 0.88 $x10^6$ cm^{-3} for KORUS-AQ. R^2 values range from 0.23 for ARCTAS-B to 0.75 for SONEX. Median ratios range from 0.66 for SONEX to 1.23 for ATom-1. Median percent differences range from -41.2% for SONEX to 20.9% for ATom-1. The fraction of times with PDs within ±40% varied from 47.3% for SONEX to 80.4% for PEM Tropics-B.

Figure 5(a) shows the HO_2 altitude profiles (red diamonds) for the common input data set. Although small differences are apparent between the full and common input set results, they

are smaller than the OH results. The PD profiles (Figure 5(b)) reveal small differences at upper altitudes for PEM Tropics-B and low altitudes for DC3 and ATom-2.

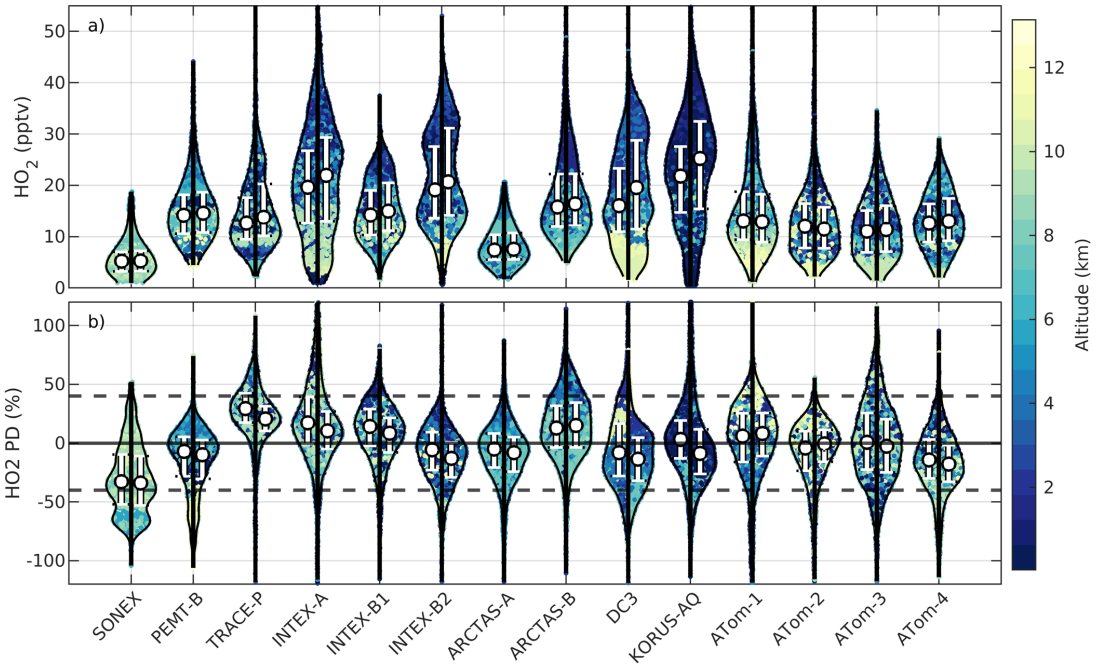

Figure 9. Violin plots of modeled HO_2, without and with common input constraints. (a) Modeled HO_2 from MCM (left violins) and MCM with common input set (right violins). The white circles represent the median and the error bars represent the model uncertainties of ±20%. (b) Percent difference between observed and modeled HO_2 using MCM (left violins) and MCM with common input set (right violins). The bars represent the 25th and 75th percentiles of PD.

Figure 9(a) shows HO_2 from MCM using the full versus common input set with, again, the largest differences between the runs occurring during missions with more frequent polluted encounters (i.e., INTEX-A, INTEX-B2, DC3, and KORUS-AQ). Similarly, changes in the distribution of HO_2 are pronounced for these missions. As for OH, HO_2 increased for most of the missions when using the common input set. The change in PDs between observed and modeled HO_2 are shown in Figure 9(b) and are well within the combined observation and model errors.

Table S3 also includes the HO_2 statistics from the common input set model runs indicated by the numbers in parentheses. The median slope, intercept, and R^2 is 0.96, 0.16 pptv, and 0.73, respectively. The median ratio and percent difference are 0.98 and -1.90%, respectively. 81.0% of the 32393 data points are within the ±40% combined uncertainties. However, the slopes range from 0.47 for SONEX to 1.59 for ARCTAS-B. Intercepts range from -6.07 pptv for ARCTAS-B to 3.85 pptv for INTEX-A. R^2 values range from 0.64 for INTEX-B1 to 0.85 for PEM Tropics-B. Median ratios range from 0.71 for SONEX to 1.23 for TRACE-P. Median percent differences range from -34.2% for SONEX to 20.6% for TRACE-P. The fraction of times with PDs within ±40% varied from 57.4% for SONEX to 92.3% for ATom-2.

4. Discussion

4.1 General agreement between observed and modeled OH and HO_2

The comparisons in the previous sections reveal that the general magnitude and behavior

of observed OH and HO_2 can be captured using the MCM model. Statistically, there is no significant benefit in using MCM over previous modeling efforts, at least in the median sense. In some cases, for both OH and HO_2, the results improve when using MCM and, in other cases, they degrade. Figure 4(a) and Figure 6(a) show similar ranges and distributions for OH and HO_2, observed and modeled, respectively. There is broad overlap in the median values, including uncertainties, for both OH and HO_2 and the median percent differences, for both OH and HO_2, along with a majority of the points, reside within the $\pm$40% range, which approximately indicates differences that are becoming statistically significant.

For all missions, nearly 15% of points reside outside the $\pm$40% range, which is only slightly more than expected from the 10% that a normal distribution has. However, TRACE-P, ARCTAS-A, and ARCTAS-B have nearly 30% of OH points outside this range. While this behavior is likely caused by the relatively low OH values encountered during these studies, the sometimes significant number of points lying outside this range indicates unexplained differences between the observations and model estimates.

The relatively poor performance for SONEX may be explained by the combination of relatively few points (556), very low OH and HO_2 values observed during this mission, and the relative immaturity of the ATHOS calibration method for SONEX, which was only the second mission for ATHOS. ARCTAS-A presents even lower OH and HO_2 values than those of SONEX but there are 2946 points available for analysis. In addition, measurement and calibration improvements for all instruments, including ATHOS, in the roughly 10 years between SONEX and ARCTAS likely contributed to the improvement for ARCTAS-A.

The behavior of HO_2 as a function of NO has been discussed in papers for several airborne and tower studies. Often, the measured HO_2 becomes increasingly more than modeled as NO abundances increase, leading to a large ratio of observed to modeled HO_2 for environments with higher HO abundances. The implication of this result is that some missing chemistry proportional to NO is cycling OH back into HO_2 (Brune et al., 2016). This effect has often been seen from towers for conditions in which the air is well mixed (Brune et al., 2016).

For airborne measurements, this effect was first observed in flights behind other jet aircraft in NASA SUCCESS in 1996 and in the Atlantic flight corridors during SONEX in 1998 (Faloona et al., 2000) (Fig. 10, SONEX points). However, a reanalysis by Olson et al. (2006) showed that this behavior could be explained by the simultaneous sampling of NO-poor, HO_2-rich ambient air along with a smaller NO-rich, HO_2-poor exhaust plumes, so that both HO_2 and NO appear to be enhanced. In the one minute for which the data were averaged in Faloona et al., the 12 km that the DC-8 flew could have sampled both ambient air and NO-rich plumes. The median HO_2 PD exhibits this behavior only for SONEX and no other mission analyzed in this study (Fig. S1), which supports Olson et al. in their assessment.

4.2 Impact of Chemical Mechanism

Even with different chemical mechanisms and input constraints, the MCM and lumped models used in previous studies produce nearly identical results for both OH and HO_2 for the SONEX through ARCTAS-B missions. The same observations used in the previous studies are used in the MCM model runs so any measurement errors will be present for all model runs using either chemical mechanism scheme. Previous analyses often point towards missing chemistry as a potential contributor to observation-to-model differences. The present results using different chemical mechanisms can't disprove this assertion as the models use similar rate constants and

any significant missing chemistry is likely missing for all the models used here.

However, this argument only holds in a median sense. The number of points residing outside the combined observation and model uncertainties suggests that some combination of observation errors and incomplete chemistry is having an impact. The tails of the PD distribution for the lumped mechanisms are broader than for MCM, indicating that MCM does a better job of representing the oxidation chemistry for some chemical regimes encountered**.** While we did not directly address the performance of the lumped models in polluted environments, differences in the distribution of OH and HO_2 values compared to the MCM model results indicate that the details of the chemical mechanism do have some importance in these environments, as has been calculated for tower-based measurements, especially when NO amounts are less than one ppbv (Chen et al., 2010).

4.3 Impact of Input Data Set

Even though the full data set has expanded over the two decades of these missions, there is no trend in the PDs for OH or HO_2 with either the full data set or the restricted common data set (Figures 4, 6, 8, 9). In addition, the PDs for the model with the full input data set is not necessarily better than that for the common data set for median values of either OH or HO_2. It should be noted that in all missions, with the possible exception of KORUS-AQ, more fairly clean air from the free troposphere was sampled than air affected by anthropogenic or biogenic emissions. The median PD values are therefore most influenced by sampling in fairly clean free tropospheric air. Thus, even the common data set is capable of simulating the oxidation chemistry of the fairly clean free troposphere.

The conclusions are very different for observations in environments affected by anthropogenic or biogenic emissions. Modeled OH tends to be lower with the full data set than with the common data set and the difference is more pronounced for INTEX-B2, DC3, and KORUS-AQ, three missions that had the most sampling in the planetary boundary layer affected by anthropogenic or biogenic emissions (Figure 8). Modeled HO_2 is also affected, but less than OH (Figure 9). These differences in OH between the full and common data sets indicate that the full data sets tend to include more chemical species that react with OH, increasing the OH reactivity and thus reducing OH. For example, during KORUS-AQ for which polluted air was more frequently sampled than during any other mission, median modeled OH is ~5.0×10^6 cm^{-3} with the full data set and ~7.0×10^6 cm^{-3} with the common data set. This difference is consistent with calculated OH reactivity, which is 19% higher in the full data set than it is in the common data set.

The PD for OH and HO_2 is shown in Figure 10 for observations compared to the MCM model with either the full data set or common data set for all nine missions. For HO_2, the PD differences are less than ~10% for all missions, as would be expected because the full and common data sets have the same HO_x sources and sinks. However, for OH, the PD differences are similar for the full and common data sets for OH reactivity below 0.5 s^{-1}, which are typical values in the fairly clean free troposphere (Thames et al., 2020). However, whereas the PD for the full data set remains near 0% for all OH reactivity values, the the PD for the common data set drops from near 0% to -40% as OH reactivity increases from 0.5 s^{-1} to 2.0 s^{-1}. This result provides more evidence that comprehensive data sets are required to successfully simulate OH and HO_2 in regions affected by anthropogenic or biogenic emissions.

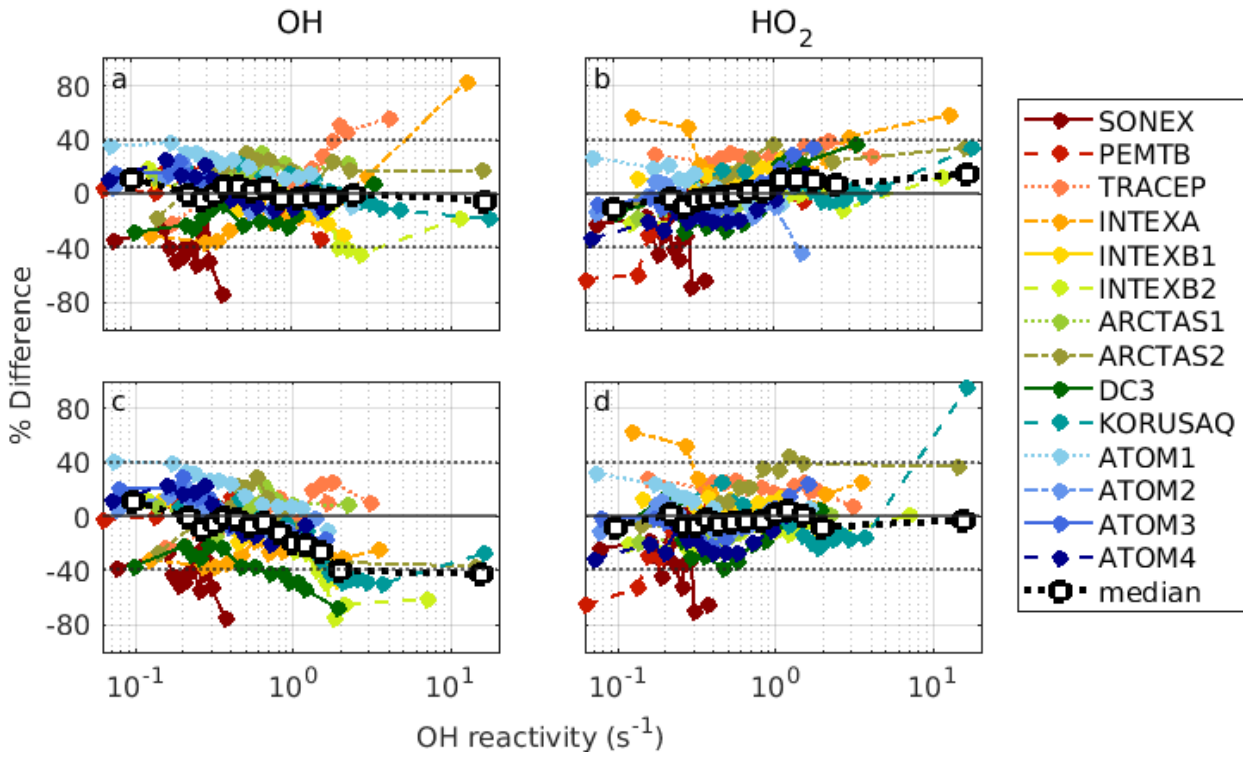

Figure 10. Percent differences (PD) of observed-to-modeled OH and HO_2. MCM with the full data set is used for OH (a) and HO_2 (b), and MCM with the common data set is used for OH (c) and HO_2 (d). Individual missions are shown, as is the median values for all missions (white-filled black circles).

5. Conclusions

This study concurs with many previous airborne studies that the general magnitudes and behavior of atmospheric OH and HO_2 can be simulated by photochemical box models. For comparing median observed and modeled OH and HO_2 in the fairly clean atmosphere, which is most of the atmosphere sampled during missions included in this study, there is no clear advantage to using a model with an explicit chemistry mechanism or a full data set. For environments affected by anthropogenic or biogenic emissions, models using explicit chemical mechanisms with full data sets perform better.

This study does not address the question "Is the current understanding of atmospheric oxidation chemistry, as determined by observed-to-modeled OH and HO_2, good enough?". However, from the results of this study, the answer is "Probably" for the fairly clean free troposphere and "Sometimes" for environments affected by anthropogenic or biogenic emissions.

From mission to mission, there are seemingly random variations in the observed-to-modeled OH and HO_2 level of agreement, statistics, percent difference distribution shapes, and altitudes of agreement and disagreement. Using a single model for all missions did not change this picture; nor did using a common data set. Here we are talking about variations occurring

from mission to mission over several years, but the same thinking applies also to short-term variations during individual flights.

This study indicates that the apparently random variations of observed-to-modeled differences in OH and HO_2 in fairly clean air are not related to model chemical mechanism or structure, but instead, result from undetected changes in instrument performance and calibration or, in some cases simply calibration error. Certainly there could be undetected changes in ATHOS performance and calibration and have been a few calibration errors that were later caught and corrected. However, it is likely that the instruments whose measurements are used to constrain the photochemical box models are also contributing to this variability. The instruments and their operators have often changed from mission to mission for many measurements, introducing one source of variability. Sometimes duplicate measurements show good agreement and sometime they do not, as happened during the four phases of ATom, when measured HCHO from one instrument was twice that for the other for the first phase but slid to only half the other for the last phase (Brune et al., 2019). These measurements and maintaining peak performance and accurate calibration are difficult.

One approach to testing the hypothesis that measurements are the cause of the observed-to-modeled variability for OH and HO_2 is to use statistical studies to establish probable relationships between deviations between observed and modeled OH and HO_2 and other measured and modeled factors. We have been begun analyzing these deviations using global sensitivity analysis to find the most influential factors and the results will be presented in a follow-up paper. A possible result is that instrument performance and calibration stability need to be improved before uncertainties in the observed-to-modeled comparisons for OH and HO_2 can be cut in half, thus enabling the detection of errors in the chemical mechanisms that are currently cloaked in uncertainty.

Acknowledgments

Support for this project comes from NASA grant 80NSSC19K1590. We thank the NASA management and aircraft personnel for their assistance and all the instrument teams whose data was used in this study. The authors declare no conflict of interest.

Author Contribution

D.O.M performed the model runs and analyzed the results. D.O.M. and W.H.B. composed the initial draft of the manuscript.

Data and Model Availability

The data and model used in this paper are publicly available:

- data:
  - SONEX: https://espo.nasa.gov/sonex/archive/browse/sonex/DC8
  - PEM Tropics-B: https://www-gte.larc.nasa.gov/gte_mrg1.htm - PEM TROPICS-B
  - TRACE-P: https://www-gte.larc.nasa.gov/gte_mrg1.htm#TRACE-P
  - INTEX-A: https://asdc.larc.nasa.gov/project/INTEXA/INTEXA_MERGES_1
  - INTEX-B: https://asdc.larc.nasa.gov/project/INTEXB/INTEXB_MERGES_1

  - ARCTAS: https://www-air.larc.nasa.gov/cgi-bin/ArcView/arctas?DC8-MERGE=1
  - DC3: https://www-air.larc.nasa.gov/cgi-bin/ArcView/dc3?MERGE=1
  - KORUS-AQ: https://www-air.larc.nasa.gov/cgi-bin/ArcView/korusaq?MERGE=1
  - ATom: https://doi.org/10.3334/ORNLDAAC/1581
- model framework: https://sites.google.com/site/wolfegm/models
- MCMv331 chemical mechanism: http://mcm.leeds.ac.uk/MCM/

References

Adhikary, B., Carmichael, G. R., Kulkarni, S., Wei, C., Tang, Y., D'Allura, A., Reidmiller, D. R. (2010). A regional scale modeling analysis of aerosol and trace gas distributions over the eastern Pacific during the INTEX-B field campaign. Atmospheric Chemistry and Physics, 10(5), 2091–2115. https://doi.org/10.5194/acp-10-2091-2010

Assaf, E., Sheps, L., Whalley, L., Heard, D., Tomas, A., Schoemaecker, C., Fittschen, C. (2017). The Reaction between CH_3O_2 and OH Radicals: Product Yields and Atmospheric Implications. Environmental Science and Technology, 51(4), 2170–2177. https://doi.org/10.1021/acs.est.6b06265

Brune, W. H., Miller, D. O., Thames, A. B., Allen, H. M., Apel, E. C., Blake, D. R., Wolfe, G. M. (2020). Exploring Oxidation in the Remote Free Troposphere: Insights From Atmospheric Tomography (ATom). Journal of Geophysical Research: Atmospheres, 125 (1), 1–17. https://doi.org/10.1029/2019JD031685

Brune, W. H., Ren, X., Zhang, L., Mao, J., Miller, D. O., Anderson, B. E., Wooldridge, P. J. (2018). Atmospheric oxidation in the presence of clouds during the Deep Convective Clouds and Chemistry (DC3) study. Atmospheric Chemistry and Physics, 18(19), 14493–14510. https://doi.org/10.5194/acp-18-14493-2018

Burkholder, J. B., Sander, S. P., Abbatt, J., Barker, J. R., Cappa, C., Crounse, J. D., Wine, P. H. (2019). Chemical Kinetics and Photochemical Data for Use in Atmospheric Studies, Evaluation No. 19 (Tech. Rep.). Pasadena: Jet Propulsion Laboratory. http://jpldataeval.jpl.nasa.gov/

Carmichael, G. R., Tang, Y., Kurata, G., Uno, I., Streets, D. G., Thongboonchoo, N., Clarke, A. D. (2003). Evaluating regional emission estimates using the TRACE-P observations. Journal of Geophysical Research: Atmospheres, 108(21). https://doi.org/10.1029/2002JD003116

Chen, S., Ren, X., Mao, J., Chen, Z., Brune, W. H., Lefer, B., Crawford, J. H. (2010). A comparison of chemical mechanisms based on TRAMP-2006 field data. Atmospheric Environment, 44(33), 4116–4125. https://doi.org/10.1016/j.atmosenv.2009.05.027

Crawford, J., Davis, D., Olson, J., Chen, G., Liu, S., Gregory, G., Blake, D. (1999). Assessment of upper tropospheric HO_x sources over the tropical Pacific based on NASA GTE/PEM data: Net

effect on HO_x and other photochemical parameters. Journal of Geophysical Research Atmospheres, 104(D13), 16255–16273. https://doi.org/10.1029/1999JD900106

Davis, D., Grodzinsky, G., Chen, G., Crawford, J., Eisele, F., Mauldin, L., Wangl, Y. (2001). Marine latitude / altitude OH distributions: Comparison. Journal of Geophysical Research, 106, 691–707. https://doi.org/10.1029/2001JD900141

Ehhalt, D. H., Dorn, H. P., & Poppe, D. (1990). The chemistry of the hydroxyl radical in the troposphere. Proceedings - Royal Society of Edinburgh, B, 97, 17–34. https://doi.org/10.1017/S0269727000005273

Faloona, I., Tan, D., Brune, W. H., Jaegl´e, L., Jacob, D. J., Kondo, Y., Fuelberg, H. (2000). Observations of HO_x and its relationship with NO_x in the upper troposphere during SONEX. Journal of Geophysical Research Atmospheres, 105(D3), 3771–3783. https://doi.org/10.1029/1999JD900914

Faloona, I. C., Tan, D., Lesher, R. L., Hazen, N. L., Frame, C. L., Simpas, J. B., Brune, W. H. (2004). A Laser-induced Fluorescence Instrument for Detecting Tropospheric OH and HO_2: Characteristics and Calibration. Journal of Atmospheric Chemistry, 47 (2), 139–167. https://doi.org/10.1023/B:JOCH.0000021036.53185.0e

Feiner, P. A., Brune, W. H., Miller, D. O., Zhang, L., Cohen, R. C., Romer, P. S., Fry, J. L. (2016). Testing Atmospheric Oxidation in an Alabama Forest. Journal of the Atmospheric Sciences, 73(12), 4699–4710. https://doi.org/10.1175/JAS-D-16-0044.1

Fuchs, H., Bohn, B., Hofzumahaus, A., Holland, F., Lu, K. D., Nehr, S., Wahner, A. (2011). Detection of HO_2 by laser-induced fluorescence: Calibration and interferences from RO_2 radicals. Atmospheric Measurement Techniques, 4(6), 1209–1225. https://doi.org/10.5194/amt-4-1209-2011

Hard, T. M., O'Brien, R. J., Chan, C. Y., & Mehrabzadeh, A. A. (1984). Tropospheric Free Radical Determination by FAGE. Environmental Science and Technology, 18(10), 768–777. https://doi.org/10.1021/es00128a009

Heard, D. E., & Pilling, M. J. (2003). Measurement of OH and HO_2 in the Troposphere. Chemical Reviews, 103(12), 5163–5198. https://doi.org/10.1021/cr020522s

Hintze, J. L., & Nelson, R. D. (1998). Violin Plots: A Box Plot-Density Trace Synergism. The American Statistician, 52(2), 181–184. https://doi.org/10.1080/00031305.1998.10480559

Jaeglé, L., Jacob, D. J., Brune, W. H., Faloona, I., Tan, D., Heikes, B. G., & Shetter, R. E. (2000). Photochemistry of HO_x in the upper troposphere at northern midlatitudes. Journal of Geophysical Research Atmospheres, 105(D3), 3877–3892. https://doi.org/10.1029/1999JD901016

Jenkin, M. E., Saunders, S. M., Wagner, V., & Pilling, M. J. (2003). Protocol for the development of the Master Chemical Mechanism, MCM v3 (Part B): Tropospheric degradation

of aromatic volatile organic compounds. Atmospheric Chemistry and Physics, 3(1), 181–193. https://doi.org/10.5194/acp-3-181-2003

Lelieveld, J., Dentener, F. J., Peters, W., & Krol, M. C. (2004). On the role of hydroxyl radicals in the self-cleansing capacity of the troposphere. Atmospheric Chemistry and Physics, 4(9/10), 2337–2344. https://doi.org/10.5194/acp-4-2337-2004

Logan, J. A., Prather, M. J., Wofsy, S. C., & McElroy, M. B. (1981). Tropospheric chemistry: a global perspective. Journal of Geophysical Research, 86 (C8), 7210–7254. https://doi.org/10.1029/JC086iC08p07210

Mao, J., Ren, X., Zhang, L., Van Duin, D. M., Cohen, R. C., Park, J.-H., & Brune, W. H. (2012). Insights into hydroxyl measurements and atmospheric oxidation in a California forest. Atmos. Chem. Phys., 12(17), 8009–8020. https://doi.org/10.5194/acp-12-8009-2012

Olson, J. R., Crawford, J. H., Brune, W., Mao, J., Ren, X., Fried, A., & Wisthaler, A. (2012). An analysis of fast photochemistry over high northern latitudes during spring and summer using in-situ observations from ARCTAS and TOPSE. Atmospheric Chemistry and Physics, 12(15), 6799–6825. https://doi.org/10.5194/acp-12-6799-2012

Olson, J. R., Crawford, J. H., Chen, G., Brune, W. H., Faloona, I. C., Tan, D., & Martinez, M. (2006). A reevaluation of airborne HO_x observations from NASA field campaigns. Journal of Geophysical Research Atmospheres, 111(10), 1–12. https://doi.org/10.1029/2005JD006617

Olson, J. R., Crawford, J. H., Chen, G., Fried, A., Evans, M. J., Jordan, C. E., & Tan, D. (2004). Testing fast photochemical theory during TRACE-P based on measurements of OH, HO_2 and CH_2O. Journal of Geophysical Research D: Atmospheres, 109(15), 1–16. https://doi.org/10.1029/2003JD004278

Olson, J. R., Crawford, J. H., Davis, D. D., Chen, G., Avery, M. A., Barrick, J. D., & Blake, D. R. (2001). Seasonal differences in the photochemistry of the South Pacific: A comparison of observations and model results from PEM-Tropics A and B. Journal of Geophysical Research Atmospheres, 106(D23), 32749–32766. https://doi.org/10.1029/2001JD900077

Ravetta, F., Jacob, D. J., Brune, W. H., Heikes, B. G., Anderson, B. E., Blake, D. R., & Talbot, R. W. (2001). Experimental evidence for the importance of convected methylhydroperoxide as a source of hydrogen oxide (HO_x) radicals in the tropical upper troposphere. Journal of Geophysical Research Atmospheres, 106(D23), 32709–32716. https://doi.org/10.1029/2001JD900009

Ren, X., Mao, J., Brune, W. H., Cantrell, C. A., Mauldin III, R. L., Hornbrook, R. S., & Singh, H. B. (2012). Airborne intercomparison of HO_x measurements using laser-induced fluorescence and chemical ionization mass spectrometry during ARCTAS. Atmospheric Measurement Techniques Discussions, 5 (2), 2529–2565. https://doi.org/10.1029/2007JD009166

Ren, X., Olson, J., Crawford, J., Brune, W., Mao, J., Long, R., & Shetter, R. (2008). HO_x Observation and Model Comparison During INTEX-A 2004: Observation, model calculation,

and comparison with previous studies. Journal of Geophysical Research - Atmospheres, 113. https://doi.org/10.1029/2007JD009166

Saunders, S. M., Jenkin, M. E., Derwent, R. G., & Pilling, M. J. (2003). Protocol for the development of the Master Chemical Mechanism, MCMv3 (Part A): Tropospheric degradation of non-aromatic volatile organic compounds. Atmospheric Chemistry and Physics, 3(1), 161–180. https://doi.org/10.5194/acp-3-161-2003

Tan, D., Faloona, I., Simpas, J. B., Brune, W., Olson, J., Crawford, J., & Singh, H. (2001). OH and HO_2 in the tropical Pacific: Results from PEM-Tropics B. Journal of Geophysical Research Atmospheres, 106(D23), 32667– 32681. https://doi.org/10.1029/2001JD900002

Wang, Y., Liu, S. C., Wine, P. H., Davis, D. D., Sandholm, S. T., Atlas, E. L., & Tan, D. (2001). Factors controlling tropospheric O_3, OH, NO_x, and SO_2 over the tropical Pacific during PEM-Tropics B. Journal of Geophysical Research Atmospheres, 106(D23), 32733–32747. https://doi.org/10.1029/2001JD900084

Wolfe, G. M., Marvin, M. R., Roberts, S. J., Travis, K. R., & Liao, J. (2016). The framework for 0-D atmospheric modeling (F0AM) v3.1. Geoscientific Model Development, 9(9), 3309–3319. https://doi.org/10.5194/gmd-9-3309-2016

York, D., Evensen, N. M., Martınez, M. L., & De Basabe Delgado, J. (2004). Unified equations for the slope, intercept, and standard errors of the best straight line. American Journal of Physics, 72(3), 367–375. https://doi.org/10.1119/1.1632486